

Nonlinear Shaping in the Picosecond Gap

Randy Lemons^{1,*}, Jack Hirschman¹, Hao Zhang^{1,3}, Charles Durfee², and Sergio Carbajo^{1,3}

¹*SLAC National Accelerator Laboratory, 2575 Sand Hill Rd, Menlo Park, CA 94025*

²*Colorado School of Mines, 1500 Illinois St, Golden, CO 80401 and*

³*University of California, Los Angeles, Los Angeles, CA 90095*

(Dated: October 29, 2024)

Lightwave pulse shaping in the picosecond regime has remained unaddressed because it resides beyond the limits of state-of-the-art techniques, either due to its inherently narrow spectral content or fundamental speed limitations in electronic devices. The so-called picosecond shaping gap hampers progress in ultrafast photoelectronics, health and medical technologies, energy and material sciences, and many other fundamental sciences. We report on a novel nonlinear method to simultaneously frequency-convert and adaptably shape the envelope of light wavepackets in the picosecond regime by balancing spectral engineering and nonlinear conversion in solid-state nonlinear media, without requiring active devices. The versatility of our methodology is captured computationally by generating a multitude of temporally shaped pulses via various nonlinear conversion chains and initial conditions. Additionally, we experimentally demonstrate this framework by producing picosecond-shaped, ultra-narrowband, near-transform limited pulses from broadband, femtosecond input pulses. Our proofs provide an avenue toward arbitrary and programmable lightwave shaping for GHz-to-THz photoelectronic sciences and technologies.

I. MAIN

Controlling the temporal profile of ultrashort laser pulses has been an active area of development since their inception in the early 1960's. The predominant techniques that have emerged to tackle this can be broadly classified as either spectral or temporal techniques. Spectral methods specialize in modulating the spectral amplitude and/or phase of broadband optical pulses, typically in the visible to near-infrared (NIR) range using devices such as spatial-light modulators[1, 2] or acousto-optic modulators[3, 4] in the Fourier plane of a dispersive element. The main limitation to utilizing spectral methods for pulse shaping is having sufficient bandwidth for the modulation devices to act upon resulting in a limitation on input pulse durations on the order of 100 fs or less. Temporal techniques directly modulate the temporal amplitude of pulses most commonly using electro-optic modulators[5, 6]. However, the time resolution with direct temporal shaping is limited by the electronic response time of the modulation devices, typically on the order of a nanosecond and above, thus limiting the application of temporal methods to pulses with similar or longer durations. Combining both spectral and temporal methods, the applicable temporal regimes do not include shaping pulses with transform-limited (TL) durations spanning from a few to hundreds of picoseconds. This is because the bandwidth of these pulses is too narrow for spectral methods and the duration too short for direct temporal methods.

Achieving efficient control of the spatiotemporal profile of pulses in this region has numerous and immediate applications. For example, certain reactions during photosynthesis have characteristic times on the order of tens of picoseconds[7] potentially opening the door for artificial photosynthesis driven by shaped optical pulses with tens of picosecond duration[8]. In semiconductors, the study of photoexcitation and charge carrier dynamics with this characteristic time[9] can be enhanced with aims towards enhancing ultrafast photoelectronic devices]. Similarly, new frontiers in picosecond duration ultrafast electronics[10] can be opened by patterning of picosecond duration pulses driving nanoplasma excitation[11]. Furthermore, x-ray free electron lasers, the brightest x-ray sources available today, are driven by picosecond duration photoexcitation laser where the spatiotemporal profile has a drastic impact on the emitted electrons and therefore x-ray generation[12, 13].

Successful shaping efforts in this picosecond shaping gap have mainly relied upon stretching femtosecond broadband pulses out to picosecond duration and modulating either the spectral amplitude[14, 15] or spectral phase[16, 17]. Once the broadband pulses are sufficiently dispersed, the temporal amplitude of the pulse can be roughly approximated by the spectral amplitude profile allowing for a linear mapping of the spectral techniques into the temporal domain. Alternatively, generating a shaped pulse from stacking many copies of few-picosecond duration pulses with increasing delay and varying amplitude has been demonstrated. While both methods are in principle suitable for achieving temporal intensity shaping in the picosecond regime, they exhibit unavoidable downsides in the form of residual spectral chirp or intensity fluctuations due to phase errors. As such, the use of pulses solely shaped by either method

* rlemons@slac.stanford.edu

is difficult or impossible in phase-sensitive or intensity-sensitive applications such as nonlinear frequency conversion, micromachining[18], and photoexcitation[19, 20] where even 5 percent deviations from expected can have drastically different measurable results.

Here we present a broadly applicable and versatile framework with experimental evidence for generating tailored temporal envelopes with (near-)TL spectral bandwidths in the picosecond regime. The baseline operating principle mixes a pair of broadband pulses that have been oppositely chirped with tailored second- and third-order spectral dispersion in a non-collinear sum-frequency generation (SFG) scheme. During the nonlinear interaction, the resultant SFG pulse is generated with a duration commensurate with the stretched duration of the mixed broadband pulses – an intensity envelope that is roughly equal to the sum of the input pulses’ envelope in the time domain – and an ultra-compressed spectral bandwidth down to the picometer. The bandwidth reduction and summing of opposite spectral chirps result in a pulse that has a remarkably low residual spectral phase noise and fluctuations, thus overcoming the limitations of any prior art. We extend beyond this baseline by adding spectral amplitude shaping onto the mixed input pulses to the SFG in addition to spectral phase control.

II. RESULTS

A. Theoretical Description

Our framework, which we have coined as dispersion controlled nonlinear synthesis (DCNS)[21], builds on the principle behind spectral compression[22, 23] wherein an initial TL broadband – e.g., few nm-bandwidth and beyond in the optical range – pulse is split into two identical copies. Here, a significant amount of equal and opposite second-order dispersion (SOD) is added to the spectral phase of each copy, and then the two are mixed in a non-collinear SFG scheme to generate a near-TL picosecond duration pulse. DCNS builds on these principles by adding third-order dispersion (TOD) to the baseline SOD when modifying the spectral phase and spectral amplitude shaping before nonlinear conversion. Unlike SOD, the added per-pulse TOD and spectral filtering are not held to the equal and opposite requirement like SOD. In theory, the SOD could also be adjusted individually, however, the nonlinear conversion efficiency is quickly reduced as the SODs of pulse pair become mismatched[24]. By including these two shaping factors for the two incident pulses, we add four additional degrees of freedom for shaping the temporal intensity profile of the SFG pulse drastically increasing the effective parameter space. For each pulse, the applied spectral phase is then a combination of both SOD (φ_2) and TOD (φ_3), where φ_2 is the primary control on pulse duration and φ_3 controls the final SFG pulse envelope shape. However, if the applied φ_2 is increased to generate a longer SFG pulse, TOD must also increase to maintain the desired shape. This relationship is linear and by defining the ratio between TOD and SOD, $\alpha = \varphi_3/\varphi_2$, the envelope duration and shape for a given input bandwidth can be described by φ_2 and α .

To generate a narrowband SFG pulse with desired shape there are two main considerations when determining the sign and magnitude of the applied phases. First, to maintain the narrowband generation requirement during SFG, the two pulses must have equal and opposite amounts of φ_2 while the magnitude is given by solving

$$\Delta t = t_0 \sqrt{1 + \left(4 \ln 2 \frac{\varphi_2}{t_0^2}\right)^2}$$

for φ_2 where Δt is the final desired duration and t is the TL input duration. Second, the sign and magnitude of φ_3 are allowed to vary based on the desired SFG temporal envelope shape. Imparting the two copies with equal magnitude and opposite sign φ_3 results in symmetric profiles while allowing either sign or magnitude to vary results in asymmetric ones. While the absolute magnitudes of the imparted phases are dependent on input bandwidth and desired shaping, a larger α implies a more significant degree of shaping and a greater departure from the input pulse shapes.

In Fig. 1 we showcase a selection of shaping possibilities with phase-only DCNS to exemplify the capabilities of this method. For each case, the shown intensity envelopes are after applying a 0.5 nm super-Gaussian spectral filter centered on the central frequency of the SFG to quench high-frequency oscillations inherent to the mixing process[SupMats]. The four scenarios that we present are (a) square-wave, (b) triangular, (c) double-hump, and (d) linear-ramp intensity distributions. Each scenario uses an input pulse with a different central wavelength and bandwidth to illustrate the applicability of DCNS to a wide range of laser systems. Of particular note are the triangular and double-hump cases for their direct applicability to high acceleration gradients in plasma wakefield acceleration[25] and emittance reduction in x-ray free electron laser facilities respectively[13, 26]. For the triangular case, the non-symmetric shape was achieved by having the same sign and magnitude of φ_3 , and therefore opposite α 's, on the two copies of the input. By having the same sign, the characteristic third-order temporal tails

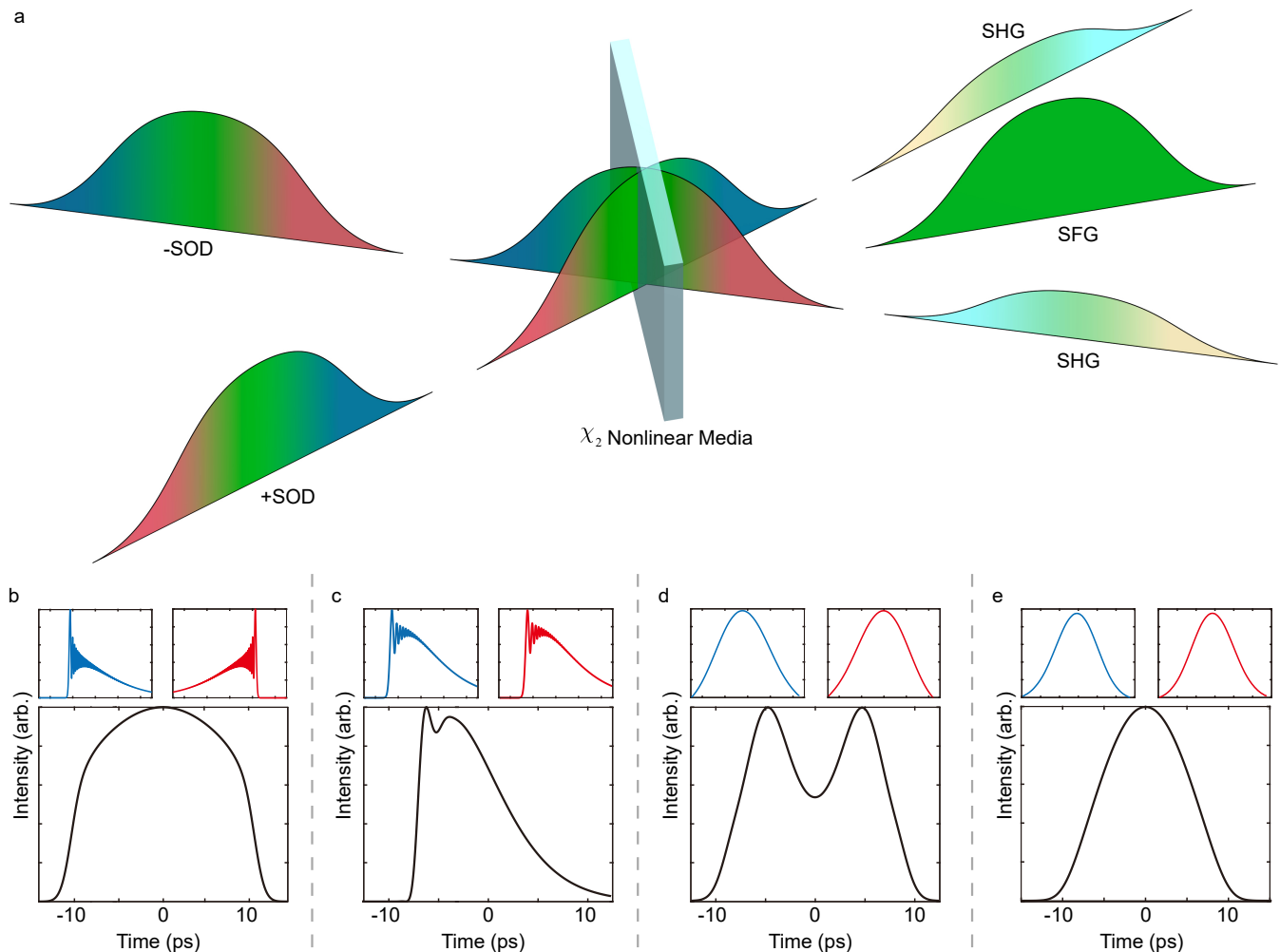


FIG. 1. (a) Conceptual representation of DCNS where two oppositely chirped broadband pulses are incident on a χ_2 nonlinear media. Two broadband chirped parasitic SHG pulses are generated along the same direction as the inputs and the narrowband near-TL SFG is generated at the mid-angle. (b-e) Four potential nonlinear shaping examples of the narrowband pulse via phase-only DCNS with varying SOD and TOD after a spectral bandpass filter of 0.5 nm. For more information on input pulse parameters and the applied spectral phase, see Supplementary Table 1.

are aligned on the same side of the main peak. In the shown example, the pulse starts with a large intensity spike, potentially useful for driving optical shockwaves, but by flipping the sign of both inputs the temporal trace can be reversed in time to resemble a gradual ramp. However, any asymmetry generated this way also results in a residual phase on the SFG pulse potentially limiting the use of these pulses to non-phase-sensitive applications. In the double-hump scenario, the two inputs are functionally identical to the square wave with equal and opposite φ_2 and φ_3 but each has been shifted by 10 ps in time relative to the other to generate an intensity void. These examples are a small subset of potentially achievable temporal profiles given the large parameter ranges of φ_2 , φ_3 , time delay, and input pulse properties and serve to illustrate the flexibility behind DCNS rather than limit potential application.

B. Experimental Phase-Only DCNS

To experimentally verify DCNS, we generated a near-TL 20 ps flattop pulse in the UV from a commercial Yb:KGW laser system producing 250 fs pulses centered at a wavelength of 1024 nm. Full details of this laser system can be found in Supplementary Note 1. To generate this temporal pulse profile, the required SOD and TOD applied to each pulse is $\pm 2.561 \text{ ps}^2$ and $\mp 0.28 \text{ ps}^3$, respectively, corresponding to an $\alpha = -.11 \text{ ps}$. The desired temporal intensity profile of the SFG after a 0.5 nm bandpass filter is shown in Fig. 1 b. This shape is similar to a higher-order super-Gaussian

pulse with a flat plateau across the central region of the pulse with rise and fall times of approximately 4 ps. These characteristics are highly sought after for reducing the emittance of photoemission-based free electron sources for ultrafast electron microscopy, high-energy physics, X-ray free electron lasers, and other secondary radiation sources.

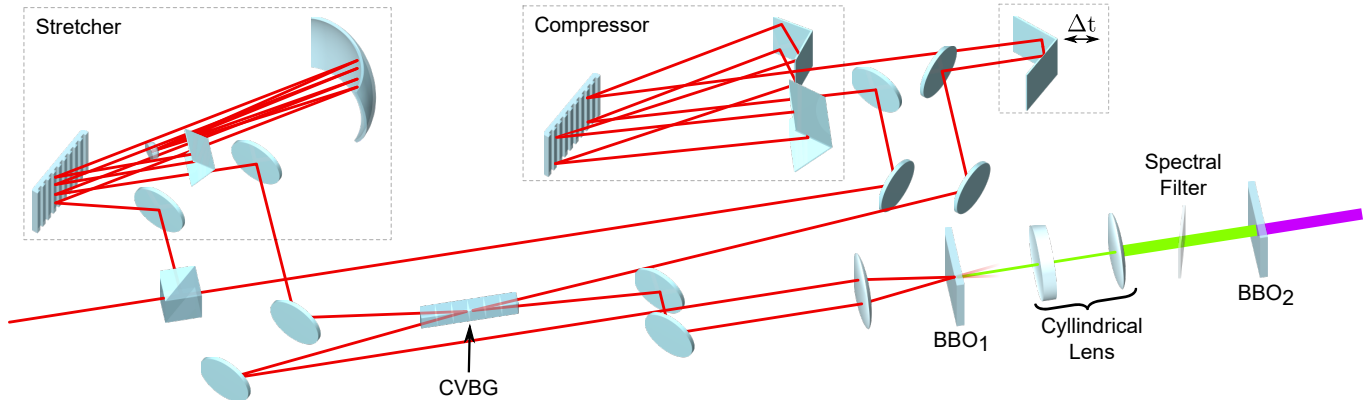


FIG. 2. Experimental layout of phase shaping and nonlinear conversion elements used for generating a flattop in the UV. A single input beam is split with equal parts going through the grating stretcher and grating compressor. Each beam is then sent into opposite ends of the CVBG, reflected internally, and finally overlapped in BBO₁ for SFG. Temporal overlap in BBO₁ is achieved through a horizontal retroreflector on a linear delay stage (Δt). The SFG beam travels through a cylindrical lens set and a spectral filter and is then converted to UV in BBO₂.

Our experimental layout (Fig. 2) is divided into two main areas: spectral phase manipulation and nonlinear conversion. The phase manipulation portion is responsible for splitting the NIR input pulse into two distinct but equal copies, referred to as the stretcher and compressor pulses, and applying the equal and opposite spectral phases. For our input parameters, achieving an $\alpha = 0.11$ with this magnitude of SOD is a non-trivial task and unachievable within a single dispersive device utilizing gratings or prisms. We avoid this limitation by combining a matched grating compressor and stretcher designed to impart significantly more SOD than desired and the proper amount of TOD with a chirped volume Bragg grating (CVBG) designed to compensate for the residual SOD of both devices. After splitting the stretcher and compressor pulses are sent through the respective single grating devices and then reflected by opposite ends of the CVBG to realize the $\pm 2.561 \text{ ps}^2$ SOD and $\mp 0.28 \text{ ps}^3$ TOD. It is important to note that the layout we have chosen for our experimental demonstration is not the only viable layout for DCNS as a framework. More sophisticated methods for manipulating the individual phase of the input pulses could be conceptualized. Examples of such solutions are distinct synchronized laser systems or pulse arrays, individualized SLMs or AOMs for the inputs, or even mixing pulses from two separate amplification systems from the same master oscillator. Ultimately, manipulation of SOD, TOD, and spectral filtering on a per-pulse basis is all that is required for DCNS.

After phase manipulation the two pulses are sent through the nonlinear conversion chain in which the SFG pulse is generated, frequency-filtered, and further converted to the fourth harmonic of the NIR input. Each nonlinear conversion step is done in a critically phase-matched β -Barium borate (BBO) crystal. In the SFG step, the two pulses are made collinear and horizontally separated then focused by a single lens onto a 2 mm BBO at an angle of 1.5 degrees to each other. Time overlap is achieved with a horizontal retroreflecting delay stage in the compressor beam path. Though both NIR inputs are spatially Gaussian with no ellipticity, the SFG beam is generated with a significant ellipticity due to the crossing angle inside the crystal. After the residual NIR and parasitic SHG pulses are discarded, this ellipticity is corrected by passing the SFG pulse through a cylindrical lens before spectral filtering. The spectral filter is angle-tuned so that the center wavelength of the filter is the same as the SFG pulse. Due to experimental limitations, we did not have a method of directly measuring the SFG temporal intensity profile; however, the narrowband and flat phase properties of the SFG pulse allow for preservation of the temporal profile through additional nonlinear conversion stages. Therefore, the SFG pulse is converted to the fourth harmonic of the NIR via degenerate collinear SHG in a 3 mm BBO where the temporal intensity profile is measured.

The UV temporal profile is measured via third-harmonic cross-correlation with a 70 fs, 1035 nm pulse from the oscillator feeding the main laser amplifier. In Fig. Fig. 3a the initial temporal profile of the UV from the above setup is shown. While this profile does demonstrate the sharp rise and fall times that were seen in the simulation, the flat central region exhibits noticeable intensity modulations. These modulations originated from an imperfection in the CVBG that removed a small amount of the long-wavelength side of the stretcher and compressor pulses. This loss of information resulted in an unbalanced contribution of the short wavelengths and thus higher frequency oscillations across the temporal profile. To correct this, we inserted a long-pass filter before the SFG focusing lens to remove a small amount of the short-wavelength side of the NIR inputs. Once the spectrum of the inputs was symmetrized, the

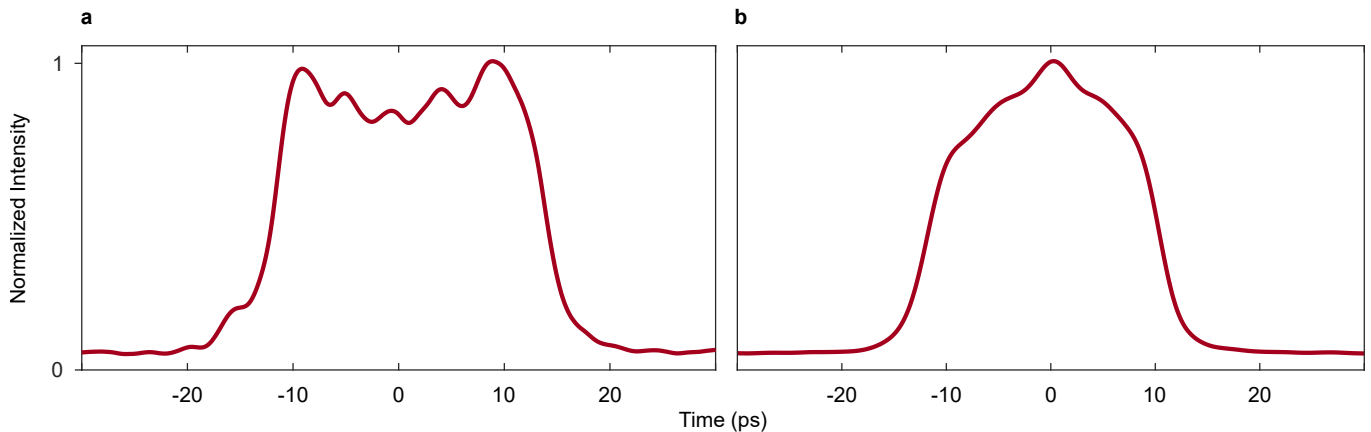


FIG. 3. UV temporal intensity profile A) without IR filtering and B) with IR filtering. IR filtering is used to symmetrize the spectrum of both inputs post-interaction with the CVBG.

resulting UV profile (Fig. 3b) drastically smoothed across the central region while maintaining the sharp rise and fall times as desired.

C. Experimental Phase and Amplitude DCNS

Correcting the UV pulse shape in this way revealed an important extension of the DCNS process towards arbitrary pulse shaping: programmable spectral amplitude filtering. In Fig. 4, we illustrate the potential of applying amplitude masking on top of a DCNS-shaped pulse. In this example, two scenarios of spectral holes being applied to the pulse with negative SOD before SFG were investigated: two spectral holes each ± 1.5 nm away from the central wavelength with widths of 0.5 nm (Fig. 4 left), and a single spectral hole with a 1 nm width at the central wavelength of the pulse (Fig. 4 right). Figure 4(a,b) are simulated results of applying these two filters to the flattop baseline DCNS pulse, and Fig. 4(c,d) are experimental demonstrations of the same spectral filters. In the case of the double hole, the envelope develops a strong intensity modulation across the central peak flanked by two small pre- and post-pulses. For the single spectral hole, the SFG pulse has a temporal profile with a deep central valley and sharply rising triangular side lobes. Experimentally, both cases are well matched in qualitative shape with the double hole generating the tri-modulated central peak with flanking sub-pulses, and the single spectral hole generating the double-peaked pulse. While the experimentally generated pulses have the same qualitative shape they are slightly longer than the simulated results. This deviation likely derives from a greater SOD and α from the matched grating pair than the SOD and α in simulation.

For both of these cases, intensity is reduced but does not go to zero at temporal locations corresponding to the location of the holes within the spectrum. While the SOD applied to these pulses is significant, especially when discussing ultrashort optics, each frequency component still temporally overlaps with those around it by some amount. As such, there is still some power within the temporal region from frequency components that haven't been filtered out. Should the magnitude of applied SOD grow, the mapping of spectrum-to-time becomes closer to one-to-one and the shaping more precise. However, this effect is muted by the spatial overlap and lack of perfect spectral filters in the Fourier plane of the compressor grating where the spectral filtering is applied. Lastly, like the baseline flattop scenario, these temporal traces are collected from in the UV rather than directly after SFG indicating that even with spectral shaping, the SFG pulse maintains its narrow-band, flat-phase nature. An intrinsic limitation of spectral amplitude shaping is decreasing the input pulse energy to such a degree that efficient nonlinear conversion in the SFG stage is no longer possible. However, by combining this with phase-only DCNS, the degree of potential shaping is extended beyond what can be achieved in shaping methods relying solely on amplitude masking for high energy or high average power applications.

III. DISCUSSION

We have described and demonstrated DCNS a new methodology that can generate pulses with tailored temporal envelope shapes in the picosecond range. By utilizing non-collinear SFG with oppositely chirped inputs, we avoid the

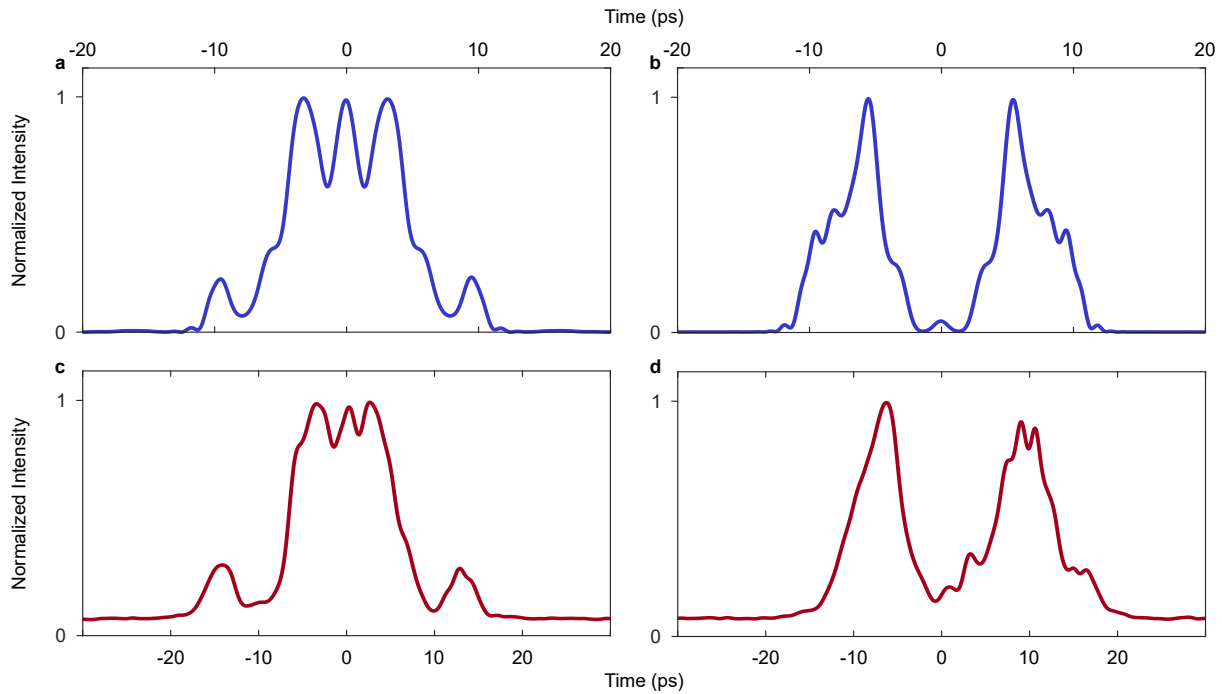


FIG. 4. Simulation of direct temporal intensity shaping during DCNS due to spectral amplitude shaping of an input pulse with a) two spectral holes, one on either side of the central frequency and b) a single spectral hole at the central frequency. Experimental spectral amplitude shaping for the c) two spectral holes, one on either side of the central frequency and d) a single spectral hole at the central frequency.

pitfalls of previous methods, such as residual spectral chirp, phase discontinuities, or unwanted intensity fluctuations, while integrating the spectral phase and amplitude shaping to enable flexibility of achievable temporal intensity profiles. As a proof-of-principle experiment based on this framework, we generated a 20 ps temporally-flattop UV pulse with little intensity fluctuations and highly compressed spectral bandwidth from 240 fs 1024 nm inputs. Additionally, we demonstrated a potential avenue toward adaptive temporal shaping through spectral amplitude modification of the broadband inputs before non-linear conversion. Our experimental implementation of DCNS is only one of many potential solutions with the most immediate improvements being found by eliminating the requirement of a CVBG for correcting large amounts of SOD. By circumventing the limitations of prior attempts at bridging the picosecond shaping gap, our method is readily deployable for a plethora of applications such as patterning of picosecond duration pulses driving nanoplasma excitation, enhancement of ultrafast photoelectron sources such as XFELs, and laser driven artificial photosynthesis.

IV. METHODS

A. Nonlinear Conversion Modeling

The dynamics involved with DCNS include laser propagation, dispersion, and nonlinear conversion in millimeter-scale nonlinear crystals and are described by the one-dimensional nonlinear Schrödinger equation [27, 28] (1D-NLSE). To model this we utilized the symmetrized split-step Fourier method (S-SSFM)[29] which oscillates between the Fourier conjugate domains of time and frequency for calculating nonlinear dynamics and dispersion respectively as the numerical method propagates along the crystal. Propagation along the crystal is handled via the angular spectrum method in the spatial frequency domain. Applying the S-SSFM to the 1D-NLSE, the governing equation for our dynamics is given by

$$A(z + dz, t) = \mathcal{F}^{-1} \left[e^{i\frac{C_D}{2}\omega^2 dz} \mathcal{F} \left[e^{iC_{NL}|A|^2 dz} \mathcal{F}^{-1} \left[e^{i\frac{C_D}{2}\omega^2 dz} \mathcal{F} [A(z, t)] \right] \right] \right] \quad (1)$$

where \mathcal{F} and \mathcal{F}^{-1} represent the forward and reverse Fourier transform respectively, A describes the pulse envelope in time, t , and space, z , C_D is the dispersion coefficient and governs the linear portion of the equation, and C_{NL} is the

nonlinear coefficient. While the linear and nonlinear portions and their effects are not separable *a priori*, the error generated in handling their effects separately is small as long as the numerical step size, dz , is sufficiently small[28].

Each DCNS scenario was modeled as the interaction between three fields, the two dispersed input fields and the SFG field with each being described individually by their respective 1D-NLSE equations. The nonlinear conversion and inter-field interactions was handled by the coupled equations for SFG[30],

$$\frac{dA_1}{dz} = \frac{2id_{eff}\omega_1^2}{k_1c^2}A_2^*A_3e^{-i\Delta kz} \quad (2a)$$

$$\frac{dA_2}{dz} = \frac{2id_{eff}\omega_2^2}{k_2c^2}A_1^*A_3e^{-i\Delta kz} \quad (2b)$$

$$\frac{dA_3}{dz} = \frac{2id_{eff}\omega_3^2}{k_3c^2}A_1A_2e^{i\Delta kz} \quad (2c)$$

where d_{eff} is the effective nonlinearity of the crystal media and Δk is the phase-mismatch between the involved fields. Our implementation of the S-SSFM calculated the full envelope of the three fields in the time and frequency domains allowing for explicitly tracking the phase mismatch between each spectral component of each field with respect to the full spectrum of the other two. As such, the monochromatic plane-wave assumptions underlying the coupled SFG equations are respected.

V. SUPPLEMENTAL MATERIALS

A. Supplementary Table 1

	Input Central Wavelength (nm)	Input Pulse Duration (fs)	Pulse 1 SOD (ps^2) and α (ps)	Pulse 2 SOD (ps^2) and α (ps)	Time Delay (ps)
Flattop	1024	246	-2.561, -0.11	2.561, -0.11	0
Triangular	800	400	2.1, 0.16	-2.1, -0.16	0
Double Hump	1550	70	0.75, -0.0036	-0.75, -0.0036	1
Linear Ramp	1064	40	0.2, -0.001	-0.2, -0.001	0

B. Supplementary Note 1

The laser system is a 40 W Light Conversion Carbide. This system can maintain 40 W of average power at repetition rates between 100 kHz and 1 MHz adjusting the pulse energy between 400 uJ and 40 uJ as required. The central wavelength is 1024 nm with a bandwidth of 8 nm at 40 uJ and 7 nm at 400 uJ.

C. Supplementary Note 2

Due to the large intensity fluctuations of the input pulses when α is high, and therefore shaping contributions from TOD is significant, the sum-frequency generated pulse also has intrinsic fast intensity oscillations. These oscillations are due to asymmetrical high-frequency spectral content on the SFG pulse. By applying a low pass filter (spectral filter) in frequency space the main temporal profile of the pulse can be retrieved while damping intensity oscillations from the high-frequency tail.

VI. ACKNOWLEDGEMENTS

We thank Michael Greenberg for his help in designing the layout of the folded stretcher and compressor, Shawn Alverson for his contributions to automation and controls integration, and Sasha Gilevich for her guidance in the setup and alignment of the cross-correlator. This work was funded by the Department of Energy Basic Energy Sciences under contract numbers DE-AC02-76SF00515 and DE-SC0022559, the Air Force Office of Scientific Research under contract no. FA9550-23-1-0409 and the Office of Naval Research under contract no. N00014-24-1-2038. Jack Hirschman would like to acknowledge support under the DoD NDSEG Fellowship.

VII. REFERENCES

-
- [1] S Yu Mironov, AK Potemkin, EI Gacheva, AV Andrianov, VV Zelenogorskii, M Krasilnikov, F Stephan, and EA Khazanov. Shaping of cylindrical and 3d ellipsoidal beams for electron photoinjector laser drivers. *Applied optics*, 55(7):1630–1635, 2016.
- [2] G Penco, E Allaria, L Badano, P Cinquegrana, P Craievich, M Danailov, A Demidovich, R Ivanov, A Lutman, L Rumiz, and et. al. Optimization of a high brightness photoinjector for a seeded fel facility. *Journal of Instrumentation*, 8(05):P05015, 2013.
- [3] Yuelin Li, Sergey Chemerisov, and John Lewellen. Laser pulse shaping for generating uniform three-dimensional ellipsoidal electron beams. *Physical Review Special Topics-Accelerators and Beams*, 12(2):020702, 2009.
- [4] Massimo Petrarca, P Musumeci, MC Mattioli, C Vicario, G Gatti, A Ghigo, S Cialdi, and I Boscolo. Production of temporally flat top uv laser pulses for sparc photo-injector. In *International Conference on Charged and Neutral Particles Channeling Phenomena II*, volume 6634, page 66341I. International Society for Optics and Photonics, 2007.
- [5] Jean-Claude Diels and Wolfgang Rudolph. 8 - pulse shaping. In Jean-Claude Diels and Wolfgang Rudolph, editors, *Ultrashort Laser Pulse Phenomena (Second Edition)*, pages 433–456. Academic Press, Burlington, second edition edition, 2006.
- [6] Mark D. Skeldon. Optical pulse-shaping system based on an electro-optic modulator driven by an aperture-coupled-stripline electrical-waveform generator. *J. Opt. Soc. Am. B*, 19(10):2423–2426, 10 2002.
- [7] Yu Guo, Lanlan He, Yunxuan Ding, Lars Kloo, Dimitrios A Pantazis, Johannes Messinger, and Licheng Sun. Closing kok’s cycle of nature’s water oxidation catalysis. *Nature Communications*, 15(1):5982, 2024.
- [8] Tomi K Baikie, Laura T Wey, Joshua M Lawrence, Hitesh Medipally, Erwin Reisner, Marc M Nowaczyk, Richard H Friend, Christopher J Howe, Christoph Schnedermann, Akshay Rao, et al. Photosynthesis re-wired on the pico-second timescale. *Nature*, 615(7954):836–840, 2023.
- [9] Christopher Perez, Scott R Ellis, Francis M Alcorn, Eric J Smoll, Elliot J Fuller, Francois Leonard, David Chandler, A Alec Talin, Ravindra Singh Bisht, Shriram Ramanathan, et al. Picosecond carrier dynamics in inas and gaas revealed by ultrafast electron microscopy. *Science Advances*, 10(20):eadn8980, 2024.
- [10] Mohammad Samizadeh Nikoo, Armin Jafari, Nirmana Perera, Minghua Zhu, Giovanni Santoruvo, and Elisa Matioli. Nanoplasma-enabled picosecond switches for ultrafast electronics. *Nature*, 579(7800):534–539, 2020.
- [11] Fenghao Sun, Qiwen Qu, Hui Li, Shicheng Jiang, Qingcao Liu, Shuai Ben, Yu Pei, Jiaying Liang, Jiawei Wang, Shanshan Song, et al. All-optical steering on the proton emission in laser-induced nanoplasmas. *Nature Communications*, 15(1):5150, 2024.
- [12] F. Zhou, I. Ben-Zvi, M. Babzien, X. Y. Chang, A. Doyuran, R. Malone, X. J. Wang, and V. Yakimenko. Experimental characterization of emittance growth induced by the nonuniform transverse laser distribution in a photoinjector. *Phys. Rev. ST Accel. Beams*, 5:094203, Sep 2002.
- [13] G Penco, M Danailov, A Demidovich, Enrico Allaria, Giovanni De Ninno, S Di Mitri, WM Fawley, Eugenio Ferrari, L Giannessi, and Mauro Trovò. Experimental demonstration of electron longitudinal-phase-space linearization by shaping the photoinjector laser pulse. *Physical review letters*, 112(4):044801, 2014.
- [14] J. Agostinelli, G. Harvey, T. Stone, and C. Gabel. Optical pulse shaping with a grating pair. *Appl. Opt.*, 18(14):2500–2504, Jul 1979.
- [15] Mark Haner and W. S. Warren. Generation of arbitrarily shaped picosecond optical pulses using an integrated electrooptic waveguide modulator. *Appl. Opt.*, 26(17):3687–3694, Sep 1987.
- [16] Betty Meng Zhang, Yujun Feng, Di Lin, Jonathan H. V. Price, Johan Nilsson, Shaiful Alam, Perry Ping Shum, David Neil Payne, and David J. Richardson. Demonstration of arbitrary temporal shaping of picosecond pulses in a radially polarized yb-fiber mopa with > 10 w average power. *Opt. Express*, 25(13):15402–15413, Jun 2017.
- [17] A. M. Weiner, J. P. Heritage, and E. M. Kirschner. High-resolution femtosecond pulse shaping. *J. Opt. Soc. Am. B*, 5(8):1563–1572, Aug 1988.
- [18] Keran Jiang, Peilei Zhang, Shijie Song, Tianzhu Sun, Yu Chen, Haichuan Shi, Hua Yan, Qinghua Lu, and Guanglong Chen. A review of ultra-short pulse laser micromachining of wide bandgap semiconductor materials: Sic and gan. *Materials Science in Semiconductor Processing*, 180:108559, 2024.
- [19] S. Bettoni, M. Csatari Divall, R. Ganter, M. Pedrozzi, E. Prat, S. Reiche, T. Schietinger, A. Trisorio, C. Vicario, and V. Goryashko. Impact of laser stacking and photocathode materials on microbunching instability in photoinjectors. *Phys. Rev. Accel. Beams*, 23:024401, 2 2020.
- [20] Chad Mitchell, Paul Emma, Ji Qiang, and Marco Venturini. sensitivity of the microbunching instability to irregularities in cathode current in the lcls-ii beam delivery system. *proceedings NAPAC2016, Oct*, pages 9–14, 2016.
- [21] Randy Lemons, Nicole Neveu, Joseph Duris, Agostino Marinelli, Charles Durfee, and Sergio Carbajo. Temporal shaping of narrow-band picosecond pulses via noncolinear sum-frequency mixing of dispersion-controlled pulses. *Physical Review Accelerators and Beams*, 25(1):013401, 2022.
- [22] F Raoult, ACL Boscheron, D Husson, C Sauteret, A Modena, Victor Malka, F Dorchies, and A Migus. Efficient generation of narrow-bandwidth picosecond pulses by frequency doubling of femtosecond chirped pulses. *Optics letters*, 23(14):1117–

- 1119, 1998.
- [23] X Ribeyre, C Rouyer, F Raoult, D Husson, C Sauteret, and A Migus. All-optical programmable shaping of narrow-band nanosecond pulses with picosecond accuracy by use of adapted chirps and quadratic nonlinearities. *Optics Letters*, 26(15):1173–1175, 2001.
 - [24] IV Kuzmin, S Yu Mironov, MA Martyanov, AK Potemkin, and EA Khazanov. Highly efficient fourth harmonic generation of broadband laser pulses retaining 3d pulse shape. *Applied Optics*, 60(11):3128–3135, 2021.
 - [25] Wei Hou Tan, Philippe Piot, and Alexander Zholents. Formation of temporally shaped electron bunches for beam-driven collinear wakefield accelerators. *Physical Review Accelerators and Beams*, 24(5):051303, 2021.
 - [26] David H. Dowell. Sources of emittance in rf photocathode injectors: Intrinsic emittance, space charge forces due to non-uniformities, rf and solenoid effects, 2016.
 - [27] N. Karjanto. The nonlinear schrödinger equation: A mathematical model with its wide-ranging applications, 2019.
 - [28] Govind P Agrawal. Nonlinear fiber optics. In *Nonlinear Science at the Dawn of the 21st Century*, pages 195–211. Springer, 2000.
 - [29] JAC Weideman and Ben M Herbst. Split-step methods for the solution of the nonlinear schrödinger equation. *SIAM Journal on Numerical Analysis*, 23(3):485–507, 1986.
 - [30] Robert W Boyd. *Nonlinear optics*. Academic press, 2019.